8-1-2012

Graphene Membranes as Electron Transparent Windows for Environmental Spectroscopy and Microscopy

Joshua D. Stoll
Southern Illinois University Carbondale, nu_eden@yahoo.com

GRAPHENE MEMBRANES AS ELECTRON TRANSPARENT WINDOWS FOR ENVIRONMENTAL SPECTROSCOPY AND MICROSCOPY

by

Joshua D. Stoll

B.S., Southern Illinois University, 2009

A Thesis
Submitted in Partial Fulfillment of the Requirements for the
Master of Science

Department of Physics
in the Graduate School
Southern Illinois University Carbondale
August 2012

THESIS APPROVAL

GRAPHENE MEMBRANES AS ELECTRON TRANSPARENT WINDOWS FOR ENVIRONMENTAL SPECTROSCOPY AND MICROSCOPY

By

Joshua D. Stoll

A Thesis Submitted in Partial

Fulfillment of the Requirements

for the Degree of

Master of Science

in the field of Physics

Approved by:

Andrei Kolmakov, Ph.D., Chair

Thushari Jayasekera, Ph.D.

Saikat Talapatra, Ph.D.

Graduate School
Southern Illinois University Carbondale
July 2, 2012

AN ABSTRACT OF THE THESIS OF

JOSHUA D. STOLL, for the Master of Science degree in PHYSICS, presented on July 2, 2012, at Southern Illinois University Carbondale.

TITLE: GRAPHENE MEMBRANES AS ELECTRON TRANSPARENT WINDOWS FOR ENVIRONMENTAL SPECTROSCOPY AND MICROSCOPY

MAJOR PROFESSOR: Dr. Andrei Kolmakov

A methodology was developed for isolation and transfer of 1-4 monolayer graphene from both Cu and Ni foil and Ni/SiO_2/Si layered substrate types for use as electron transparent windows in environmental electron microscopy and spectroscopy. The graphene membranes were transferred onto disc “frames” made of stainless steel containing 3-10 μm diameter apertures. Such frames “windowed” with the graphene membrane are assembled into the custom designed environmental cell (e-cell) which contain a specimen immersed in the desired liquid or gaseous environment, and are compatible for imaging with a conventional scanning electron microscope (SEM) (in this case, a Hitachi 4500 SEM). Gold nanoparticles (50 nm) colloidal in water served as model specimens and were observed inside the e-cell using both secondary electron and backscattered electron detectors. An imaging induced radiolysis of water was observed at higher electron doses, which manifested itself in the formation of bubbles growing and coalescing under the enclosed graphene surface. Key SEM imaging parameters responsible for driving the radiolysis phenomena were addressed.

ACKNOWLEDGMENTS

The findings presented in this paper as well as its construction could not have been completed without the help of many people. I first and foremost would like to acknowledge my research advisor, Dr. Andrei Kolmakov, for acceptance into his research team and for exposure to his challenging and demanding field of research. Other members of the research team are also due acknowledgment; Dr. Evgheni Strelcov, Ms. Jie Zhang, and Mr. Daniel Mallernee. Special thanks are due to Mr. Mallernee for his assistance and time spent towards providing instruction concerning laboratory equipment and techniques.

I would also like to thank Dr. Saikat Talapatra and Dr. Thushari Jayasekera for serving as members of my defense committee. Dr. Talapatra's patience and assistance that he provided while serving as graduate advisor should also be acknowledged. I would also like to acknowledge Dr. Naushad Ali for providing adequate time to complete the work presented in this paper.

Acknowledgements are also due to Mr. Clay Watts for his assistance in developing some of the technology utilized in this paper and also Mr. Robert Baer for his maintenance and repair of the research laboratory computers. Furthermore, I would like to acknowledge the office systems specialists, Mrs. Suzanne McCann and Mrs. Sally Pleasure, who made sure all paperwork was completed prior to deadlines and reached the correct destination.

TABLE OF CONTENTS

LIST OF TABLES

LIST OF FIGURES

CHAPTER 1

INTRODUCTION

1.1 Background

Electron microscopy and spectroscopy at solid-liquid-gas interfaces is fundamental to understanding dynamic physical and chemical processes of matter at and beyond the nanoscale but currently is not widely available due to high cost and limited availability of the technology. Standard electron microscopes and spectroscopes require vacuum conditions, therefore the development of disposable environmental cells (e-cells) allows for multi-phase non-vacuum pressure imaging with Transmission Electron Microscopy (TEM), Scanning Electron Microscopy (SEM), Scanning Transmission X-Ray Microscopy (STXM), Scanning Photoelectron Microscopy (SPEM), Scanning Auger Microscopy (SAM), and all optical microscopy as well [1, 10, 20, 21, 38]. With this study, we focus on the e-cell design relevant to SEM, although it can be compatible with all aforementioned microscopy and spectroscopy techniques.

With recent advances in characterizing structural, electrical, and chemical properties of graphene, procedures have been developed to achieve mass production of high quality grown monolayer, bilayer, and multilayer graphene with a precise number of layers and a high degree of surface

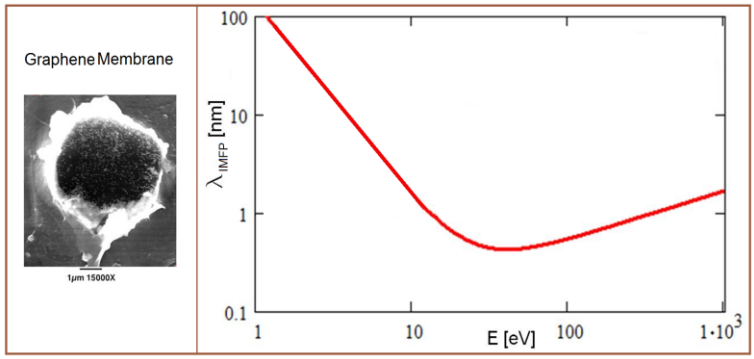

Figure 1. (left) SEM image of an orifice covered with a graphene membrane. The membrane isolates a water solution of 50 nm Au NP from the vacuum of the SEM. (right) The calculated inelastic mean free path of electrons in graphite as a function of the electron's energy is plotted [32].

Table 1

Electron energies and their respective λ_{IMFP} values in graphite: the λ_{IMFP} values have been chosen to correspond to the thickness of three and four graphene monolayers [14, 24, 39].

Determination Method	Effective # of Graphene Monolayers	λ_{IMFP} (Å)	Energy (eV)
Optical Data or Predictive Formula	3	10.05	253
	4	13.4	390
Predictive Formula	3	10.05	521
	4	13.4	766
Experimental Data	3	10.05	372
	4	13.4	545

uniformity [3, 7, 16, 23, 28, 29]. Graphene has material properties excelling in mechanical strength and electron transparency as well as being impermeable to liquids and gases [4, 37]. Based on the estimation of the electron mean free path in graphite (Figure 1, Table 1), even a three monolayer thick graphene (ca 1.2 nm thick) membrane will be nearly transparent to electron with kinetic energies (KEs) as small as 300 eV. In order for graphene to be a potential candidate for electron microscopy or spectroscopy, the transparency of the graphene window must be sufficient to achieve a high probability for an electrons passage through the window and ultimately to the sample or detector. This requirement is fulfilled with the inelastic mean free path (λ_{IMFP}) of electrons in graphite combined with the KEs required to achieve their respective values of λ_{IMFP}, which is defined as the average distance an electron with a specified kinetic energy (KE) travels through a certain media before losing an amount of energy equal to $1/e$ multiplied by the electron's initially specified KE. More explicitly, the following equation relates λ_{IMFP} to the probability for electrons of a specific KE to be transmitted a certain distance through a specific material.

$$I(d) = I_0 \, e^{(-d \,/\, \lambda(E))}$$

Consider now a beam of electrons for the previous equation, where I(d) represents the intensity of the electron beam as a function of the distance, d, the beam

travels through its respective media, with I_0 being the beam's initial intensity. Bulk graphene, or graphite, is composed of staggered stacks of graphene monolayers separated by a ~3.35 Å interplanar spacing [42]. Thus, three monolayer and four monolayer sheets of graphene would form functional thicknesses of ~10.05 Å and ~13.4 Å, respectively. Thus, an electron beam with an energy in the range of 253-521 eV would transmit, on average, 63% of the electrons through three graphene monolayers. This range of KE for electrons lies near the lower limit of electron beam energies currently used in SEM, thus tri-layer graphene becomes transparent to primary electrons (PEs), as well as appreciably transparent to some of the secondary electrons (SEs) and backscattered electrons (BSEs) used for image formation even at lower PE beam energies. Further increasing the energy of the PE beam improves the transparency of the given membrane to the PEs and BSEs. With this level of electron transparency, graphene can act as a unique window in a containment cell hosting a non-vacuum environment to be imaged with SEM [20, 21]. After data collection, the low cost e-cell can be disposed of after either a single use or multiple uses, depending on the stability and integrity of the graphene membrane and post-use contamination of the e-cell.

The advance of electron microscopy methods beyond traditional optical microscopy has allowed scientists to observe objects in their native environment at a nanoscopic level well beyond that which could be achieved with a diffraction-limited optical microscope. With the use of high energy electrons as the imaging probe, much smaller diffraction-limited wavelengths can be achieved. Electron irradiation of the imaged sample can also reveal its electrical conductivity and its chemical composition.

The topological image, chemical composition, and electrical conductivity can then be deciphered from electron and photon signatures collected from the irradiated sample. This principle, the basis of electron microscopy, was first implemented by Max Knolls and Ernst Ruska in 1931 when they successfully obtained an image using the first, self-constructed electron microscope [15].

Currently, standard SEM utilize a focused beam of high-energy PEs typically in the range of 0.5 keV to 30 keV, with the dry sample imaged under high vacuum conditions and commonly sputter-coated with few nanometer gold layer if it is not electrically-conductive. With the PE beam in this energy range, the electrons will exhibit a de Broglie wavelength between 8.7×10^{-11} m and 6.0×10^{-12} m, the latter being more than 10,000 times smaller than the shortest wavelengths of visible light. Lensing, scanning, and signal retrieval in SEM is controlled via manipulation of magnetic fields. The smaller wavelength of the electron beam coupled with non-diffractive magnetic lensing allows for magnification of more than 500,000 times, exceeding that which is possible with optical microscopes by about 500 fold.

When operating under high vacuum, the PE beam and resultant signals from the imaged object avoid unwanted interactions with gases in the sample's environment. As a result, only dry, solid, electrically-conductive objects can be routinely imaged with standard non-environmental electron microscopy and spectroscopy technology. Advanced differential pumping stages in the column of the SEM resulted in Environmental Scanning Electron Microscopy (ESEM) which allows imaging in gaseous environment up to few Torr of pressure [9].

Technology is currently available commercially for SEM in wet environments by use of a containment cell with an electron transparent window [8]. Coined El-Mul (QuantomiX) WETSEM®, the e-cell is able to withstand pressures up to 1 atmosphere and allows imaging of wet samples and liquid environments at atmospheric pressure [21]. The ~150 nm thick polyimide membrane is impenetrable for liquids that are compatible with the e-cell, and the e-cells are low-cost and single-use disposable.

The capabilities of graphene-oxide (GO) as electron transparent windows for e-cells have been shown previously in obtaining SEM images of 50 nm gold colloid nanoparticles (NP) [20, 21]. The NP were enclosed in an e-cell under atmospheric pressure and a GO membrane was suspended over a 3-10 μm viewing orifice to function as the electron transparent window [20]. Due to the robust nature of GO, the e-cell window maintained integrity during imaging under high vacuum conditions and exhibited a high transparency for the incident electron beam and the outgoing electrons used as spectral and imaging signals. Clear images revealing the sizes and shape of individual NPs on the outer perimeter of aggregated islands on the inner surface of the GO window were obtained. Due to functional similarities between GO and graphene, the latter material also proves to serve well as a candidate for electron transparent window material for use in e-cells and imaging under high vacuum conditions. With its decreased thickness and possessing fewer structural defects, graphene is going to be even more promising as a robust electron transparent membrane in comparison to GO. The latter success with GO windows motivated the research findings put forth in this paper.

1.2 Theoretical Simulations

To observe how graphene competes with other materials also implemented as electron transparent windows in e-cells, a free Monte Carlo simulation program, Casino v2.48 [12], was used to calculate theoretical contrasts for imaging a model 50 nm gold layer submerged at varied depths in water behind graphene, silicon nitride, and QuantomiX (Kapton polyimide) membranes. The Casino software simulates single electron trajectories in 2-dimensional layered materials incorporating elastic and inelastic scattering effects dependent on the material's elemental composition and density. Through Monte Carlo simulation, the electron backscattering coefficient (BSC) of the layered material under the specified simulation conditions can be determined. Membrane specifics concerning thickness, density, and chemical composition are listed in Table 2. The contrasts for each membrane were plotted as a function of Au depth

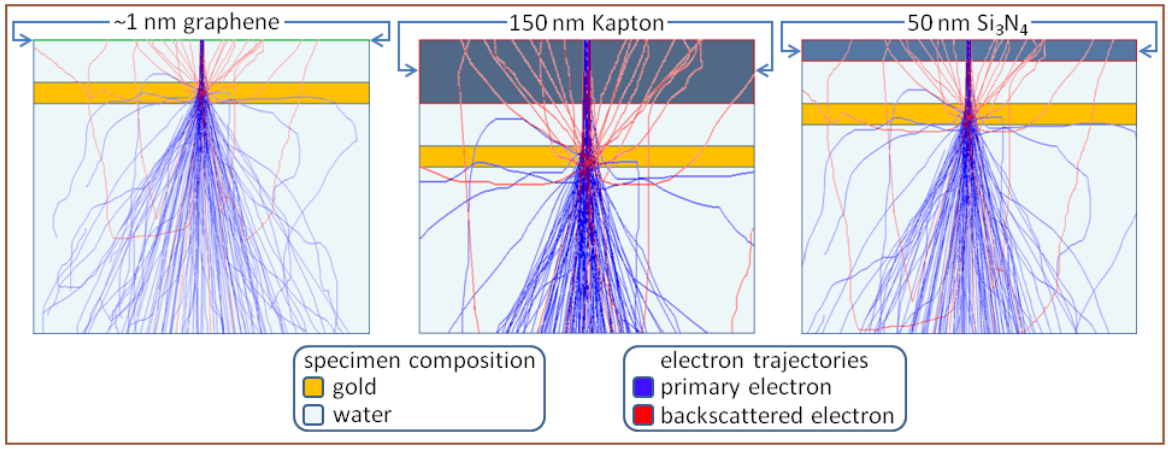

Figure 2. The Casino software simulated electron trajectories for 2-dimensional, layered materials. These layered-type configurations would be input into the Casino software as model parameters to simulate SEM imaging of a 50 nm gold layer in water at the specified depth behind the respective membrane (shown roughly to scale for a 100 nm submergence depth in water). The simulated PE trajectories from the SEM are represented by the blue lines and the backscattered electrons by the red. These scattering patterns are typical for a 20 keV PE beam incident on the Au/H_2O specimen, although the displayed electron trajectories shown above were reproduced to only mimic those of the Casino software and do not actually take into account the effect of the membranes in these particular representations.

behind the membrane, with the minimum depth equivalent to gold existing at the back surface of the membrane. Five Casino simulations were conducted for each data point plotted in the graphs within Figures 3 and 4, with the upper/lower limits of the error bars defined as the *mean of contrasts* +/- *absolute deviation*, respectively. The contrast, C, for each point has been calculated using the following formula:

$$C = \frac{\left|S_{Au} - S_{H_2O}\right|}{S_{Au} + S_{H_2O}} ,$$

where S represents the respective material's electron BSC. More explicitly, S_{H20} corresponds to the BSC for water behind the respective membrane at the specific scanning energy, while S_{Au} represents the BSC achieved for the model 50 nm thick Au layer scanned at the respective specific scanning energy behind both the corresponding membrane and a layer (depth) of water, with a water substrate composing the remainder of the sample volume behind the Au layer (Figure 2). Values for the BSCs were collected for PE beam energies of 5 keV, 10 keV, 20 keV, and 30 keV, with the only other alteration to default settings in Casino's microscope setup options being the number of electrons simulated, which was set at 10,000 electrons per simulation.

Table 2
Characteristics of membranes used in Casino SEM simulations: values for the density of graphene [27], silicon nitride [25, 36], and the QuantomiX polyimide [18], as well as the specific chemical composition of the latter membrane [33, 40] were input into the sample settings within Casino to determine how the materials compare as electron transparent windows. The thickness for graphene corresponds to 4 monolayers, whereas thicknesses for the silicon nitride and QuantomiX membrane were chosen to be representative of commercially available membranes used for similar vacuum level imaging conditions.

Membrane Type	Chemical Formula	Density (g/cc)	Thickness (nm)
Graphene	C	2.25	1.34
Silicon Nitride	Si_3N_4	3.211	50
QuantomiX	$C_{22}N_2H_{10}O_5$	1.42	150

Operator settings concerning distributions, runtime options, and physical models within the program were maintained at the defaulted options. The Au layer was specified to be 50 nm thick to correlate to imaging a 50 nm Au NP suspended in water, as a colloid of the latter NPs and water composed our sample specimens during actual SEM imaging utilizing our e-cell. The optimum relative transparency for graphene is most evident due to the greater relative differences between the membrane's and the imaged specimen's BSC, since this difference in the BSC defines the contrast in the image when using the backscattered electron detector (BSED). The latter relative differences in BSC's for a 50 nm Au layer in water increases to a maximum at the lower SEM imaging energies (Figure 3) and at minimal distances from the membranes where the electron "braking effect" due to the increase in cumulative inelastic scattering arising from the increasing thickness of the water layer between the membrane and the Au layer has not yet developed to a

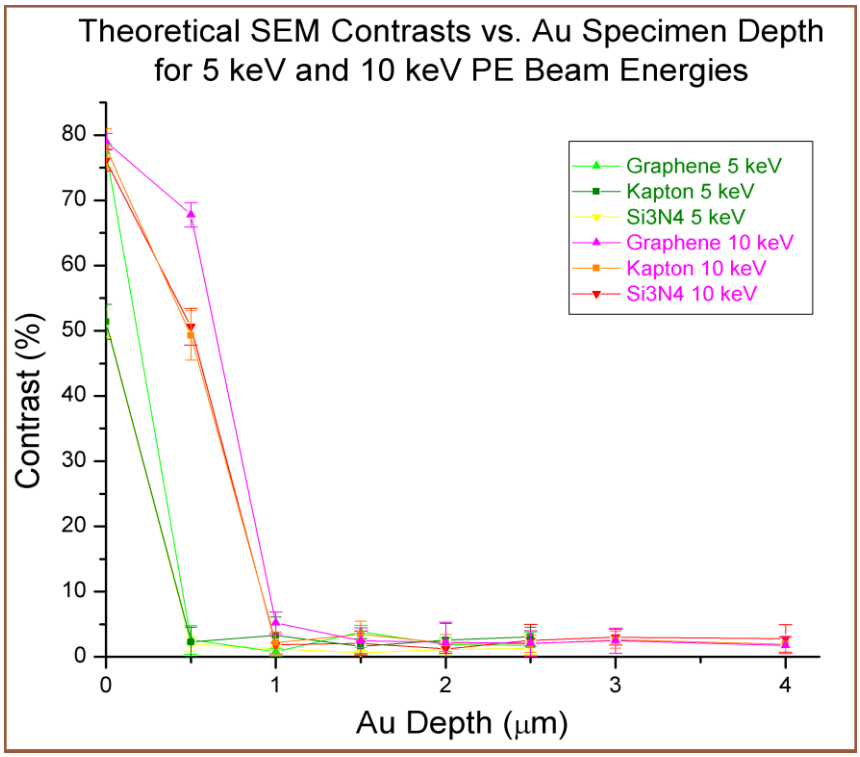

Figure 3. Results from Casino [12] simulations for comparison of theoretical image contrasts between graphene, silicon nitride, and QuantomiX (Kapton) membranes at 5 keV and 10 keV beam energies: The graphene membrane is observed to outperform the other two membranes most noticeably at the 5 keV PE beam energy and in the contrast transition regions at the points for which highest negative gradients of the slopes for graphene are evident.

considerable degree. Upon reaching a point where BSEs emanating from the Au layer no longer reach the BSED, the imaged specimen will be observed solely as a homogenous bulk volume of water (omitting potential vapor production due to induced water radiolysis initiated by the PE beam). At higher PE beam energies (Figure 4), the increasing thickness of the water layer is primarily responsible for determining whether or not a sufficient number of BSEs deflected by the Au layer reach the BSED due to the three membrane materials and the water being more similarly transparent to 20 keV and 30 keV electrons; thus, scattering effects induced by the membrane materials at the latter energies become negligible relative to those induced by the water layer interlaid between the membrane and the Au layer.

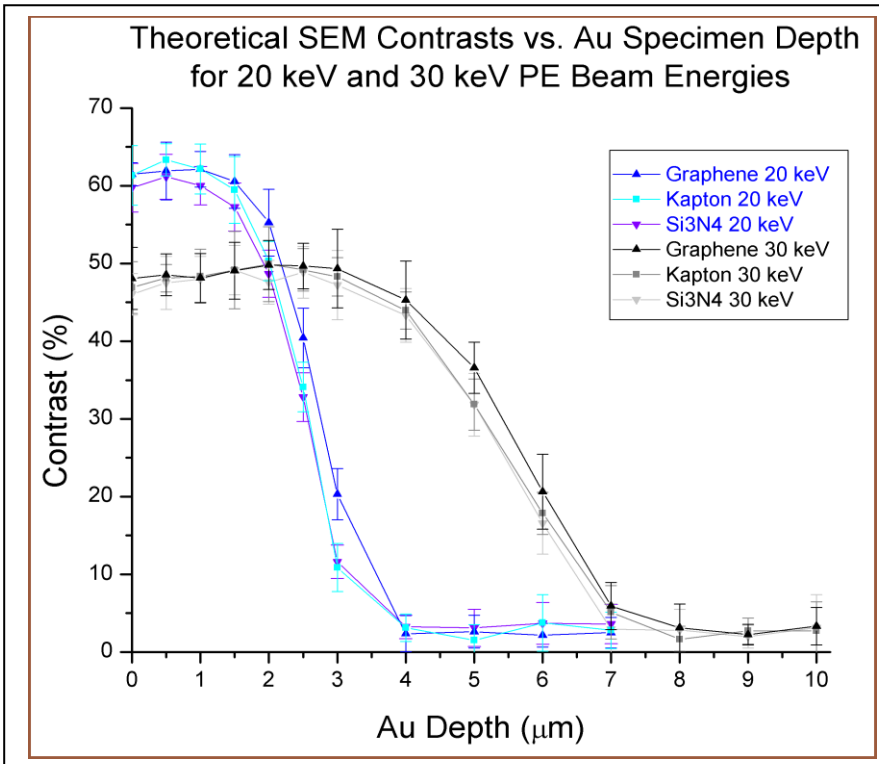

Figure 4. Results from Casino [12] simulations for comparison of theoretical image contrasts between graphene, silicon nitride, and QuantomiX (Kapton) membranes at 20 keV and 30 keV PE beam energies: all three membranes provide roughly equivalent image contrasts at the 20-30 keV beam energies.

CHAPTER 2

EXPERIMENTAL

2.1 Graphene Samples

Graphene samples were purchased from Graphene Supermarket (graphene-supermarket.com) in two layered configurations as seen in Figure 5. The graphene layers were formed through low-pressure chemical vapor deposition (LPCVD) of carbonaceous gases on growth substrates of either 20um thick foils (Figure 5a) of Cu (monolayer graphene) and Ni (multilayer graphene) or 300 nm thin film of Ni deposited on SiO_2/Si wafer (Figure 5b). Prior to LPCVD, the foil or thin film growth substrates are subjected to a low pressure high temperature (900°-1000° C) annealing and reduction procedure, typically flowing a solitary or mixture of gas(es) of hydrogen, argon, and nitrogen to assist in reduction and heat transfer [3, 16, 23, 28, 29]. The annealing/reduction procedure increases grain size and removes oxides from the surface [29], allowing for better catalytic activity between either Ni or Cu and the carbon and thus lowering the growth temperature needed for breaking hydrocarbon bonds of the precursor gas [23]. The pressure during annealing/reduction and subsequent growth for LPCVD of graphene is maintained in the range of 0.1-20 torr [3, 16, 23, 28, 29], with varying growth times anywhere from 20 s to 30 min and 20 s to 60 min for

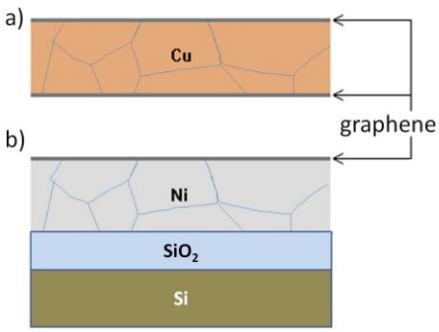

Figure 5. Two different kinds of substrate layouts for graphene samples: a) monolayer/multilayer graphene on Cu/Ni foils (shown above on Cu foil); b) multilayer graphene grown on Ni/SiO_2/Si wafer. The level of defects within the graphene layer(s) is dependent on the domains within the foils and metal thin films.

growth on Cu and Ni, respectively [3, 16, 23, 28]. The growth phase is initiated by the introduction of hydrocarbon group containing gases such as methane or acetylene [3, 7, 16, 23, 28, 29], possibly along with slight variations in temperature and pressure relative to the initial annealing stage, with growth temperatures and pressures within the range of 890°-1000° C and 0.1-20 torr, respectively [3, 23, 28, 29]. Once the growth stage is complete, the substrates are cooled under flow of single component or a mixture of gases mentioned previously as being used in the annealing/reduction stage [16, 23, 28, 29].

Graphene forms on both Ni and Cu due to its lattice matching with that of the latter metals (Figure 6), yet it is the relative variation in the solubility of carbon in Ni and Cu that provides the differentiation between growth of single- and multi-layer graphene. With carbon's low solubility in Cu [28] and relatively much higher solubility in Ni, predominately monolayer graphene forms on Cu and graphene stacks form on Ni, sometimes exceeding 10 layers [23]. Surface adsorption of precursor gases on both Ni and Cu drives the initial graphene monolayer formation. The observance of pre-dominantly multilayer graphene grown on Ni is due to the variation of carbons solubility in Ni when cooling from the high growth

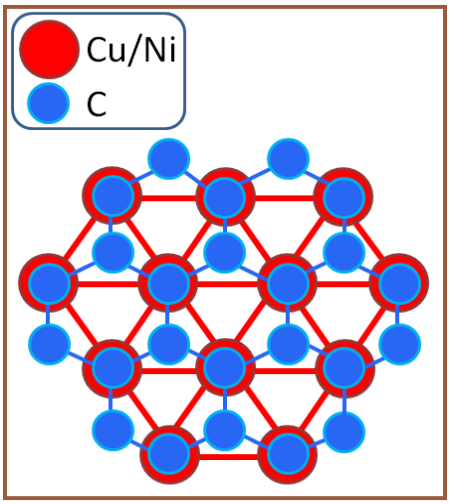

Figure 6. There is only a slight lattice mismatch between Graphene's (001) plane (a = 2.46 Å) and the (111) plane of Cu/Ni (a = 3.62 Å / a = 3.52 Å) in the crystal lattice arrangement seen above [6, 41, 43]. Graphene's crystalline structure consists of hexagonal sheets in the (001) plane while both Cu and Ni arrange in FCC crystalline structures. The percent error in lattice matching for Graphene relative to its latter stated primitive lattice vector is +4.02% and +1.14% with Cu and Ni, respectively. Thus, modifying graphene's stated primitive lattice vector by the latter percentages would yield perfect lattice matching in the above orientation.

temperature to room temperature in addition to the latter growth mechanism [3, 7, 23]. Multilayer growth of graphene can occur on Cu up to three layers thick, but is isolated. Extending growth times in pursuit of large domains of multilayer graphene on Cu only results in the formation of pyrolytic carbon on top of the graphene monolayer due to the lack of catalytic activity between graphene and the carbon precursor gas [23].

2.2 Graphene Transfer Protocol

Graphene grown on both Ni foil/film and Cu foil were utilized for fabrication of the e-cell window specified as maintaining thickness's of 4 and 1 monolayer's, respectively. Two transfer protocols were developed, one for isolating graphene from the foils and the other for isolating graphene from the thin metal film on SiO_2/Si wafer.

Transfer of the graphene membrane from the foils was approached by first carefully cutting 3x3 mm square segments of the graphene-Cu or graphene-Ni foils (Figure 7 (a)). The foil segments were then made planar by compressing the segments between two clean glass microscope slides (Figure 7 (b)). The segments were then inspected under an optical microscope to determine which side contained minimum

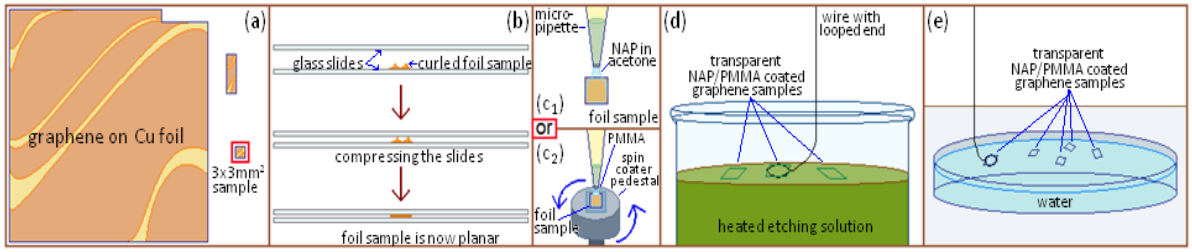

Figure 7. Initial steps for isolating graphene from the foil substrate: (a) the process began with first cutting out small 3x3 mm^2 segments of foil, then (b) compressing the foil segments to flatten them. The minimally defected face of the foil was then either (c_1) drop-casted or (c_2) spin-coated with a polymer, forming a thin protective layer for the delicate graphene during subsequent processing. (d) The metal foil was chemically etched away, leaving small clear segments of polymer/graphene remained floating on the surface of the etching solution. The clear segments were gently removed from the etching solution and (e) placed to float on the surface of distilled water.

facial defects and scratches. The optimal side was then either drop-coated or spin-coated with a protective polymer layer (Figure 7 (c_1), (c_2)).

Two types of polymers were used as protective films to shield the optimal graphene side of the foil segment from further damage and contamination during the next fabrication steps. Only a single type of protective layer was used per individual foil segment, with two types of approaches for polymer removal being initiated in order to explore which approach would yield the cleanest graphene surface after removal of the polymer, as well as which approach would incur the least amount of damage to the graphene. The first type of protective layer was composed of fine layer of Poly(methyl methacrylate) (PMMA) and was spin-coated over the optimal surface of graphene (Figure 7 (c_2)), adopting this procedure from the following reference [22]. The spin-coater settings were calibrated to yield a very fine layer of PMMA of uniform thickness across the deposited surface. In order to produce the desired surface coating, the spin-coater (Metron Systems Inc.) settings for acceleration and speed were set to maximum and 6500 rpm, respectively. Maximum rotational speeds were reached within ~1 s. For the second type of protective layer, a 2 μl volume from a 1:10 solution of clear nail polish (NAP) and acetone, respectively, was dropcasted with a micropipette (Figure 7 (c_1)) and set aside for ~10 min to dry in air. With the acetone fully evaporated, a 5-50 micron layer of NAP remained to serve as the protective film.

Once the protective layer had cured, the foil segments were then placed on a low-lint delicate-task tissue paper (LDTP) with the protective layer facing down. The side facing up was then delicately scratched with an X-ACTO® knife to expose the back side of the foil still containing the as-grown graphene multilayer to the chemical etchant.

The following reference, [22], was again utilized for the type, concentration, and temperature for the etching procedure. The foil segment was placed to float on the surface of a 1 M $FeCl_3$ aqueous etching solution with the scratched side in contact with the surface of the solution. The etching solution was warmed on a hot plate and maintained at ~65° C during the etching process which typically took between 0.5-1 hr for 25 micron foils. When the floating segments became free from metal and transparent, they were removed from the etching solution with the aid of a piece of nickel wire with a small loop at the end ~3 mm in diameter (Figure 7 (d)). The segments were then placed to float on the surface of distilled water with the protective layer still facing up, diluting any remnant etching solution transferred with the segment (Figure 7 (e)). With the metal growth substrate removed, only the minimally-defected graphene layer and its protective polymer film remained to compose the now transparent segment.

The procedure for removing graphene from $Ni/SiO_2/Si$ is similar to the one used for removing graphene from Ni/Cu foils with only slight alterations to the initial steps in

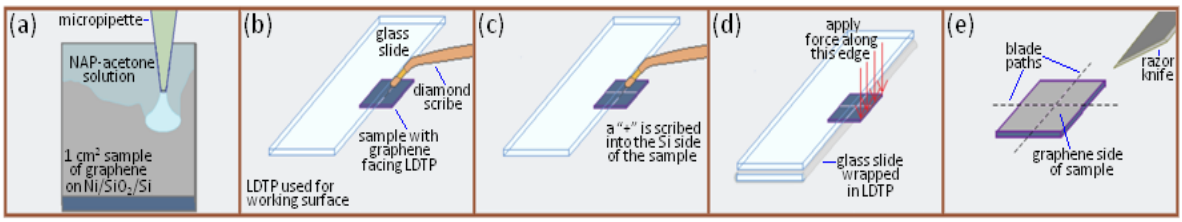

Figure 8. Initial steps for isolating graphene from $Ni/SiO_2/Si$ substrates: (a) first, a NAP protective layer of NAP was applied to the delicate graphene surface. (b), (c) With the aid of a glass slide, a diamond scribe was used to create two fracture lines in the Si side in an orientation which divided the sample into square quarters. (d) Then, by putting the sample between two glass and by applying a force laterally along the edge indicated by the red arrows, a break occurred along the fracture line currently flush with the edges of the glass slides. This was repeated for the remaining fracture line, and (e) with the polymer layer still intact, the sample was turned over and with an X-ACTO® knife, incisions were made along the dashed lines to produce four isolated sections sized appropriately for subsequent chemical etching and deposition onto the final substrate.

the protocol, the details of which are elaborated upon in Figure 8. Upon coating the graphene surface with a layer of NAP and processing samples to an appropriate 3x3 mm^2 size, the samples were then submerged in a heated $FeCl_3$ etching solution. Once the Ni was etched away, effectively isolating the NAP coated graphene from the substrate so that it could float freely in the etching solution, it was handled as before in a manner similar to that which was used with processing graphene on the metal foils, with the segments being transferred to float on the surface of distilled water (Figure 7 (d), (e)).

The graphene segments were then placed on the final substrates which serve as the primary frame for the viewing window. The final substrates were 9.5 mm diameter 100 micron thick stainless steel 304 (SS304), electrochemically polished flow control orifice discs (ODs) containing 3-10 μm holes laser drilled through their centers (Lenox Laser Inc). The ODs were analyzed under a microscope to determine which side contained the face incident to the laser during the drilling procedure as this side contains an orifice surface perimeter more suitable for suspension of the graphene membrane. The face from which the laser exited contained an orifice typically with a larger entrance diameter than the incident face as well as surface darkening along the perimeter, indicating the potential for increased surface roughness and decreased van der Waals interaction between the graphene membrane and the surface of the OD. The smaller entrance diameter to the orifice was preferred for membrane deposition as with an increasing surface area that is interfacing the vacuum and cell environment, a corresponding linear increase in force is applied to the membrane for the same relative pressure difference on either side of the membrane ($P = F/A$). Thus, the survivability

of membranes has a tendency to decrease as orifice entrance diameter increases [22]. The ODs were labeled with a letter for identification with small navigation scratches made to the laser-incident face. A small circle with crosshairs, centered on the orifice, was scratched in on the same face so the orifice could be found easily with SEM as it was not visible by the naked eye. Careful attention was paid so as not to make scratches near the perimeter of the orifice which would disrupt van der Waals interaction and inhibit the formation of a vacuum seal between the graphene membrane and the perimeter of the orifice.

To place the segments on the ODs, the latter were dipped into the distilled water still floating the segments which were "fished" out by slowly lifting the ODs vertically out of the distilled water with the segments centered above the OD's orifice (Figure 9 (a)). The effectively windowed frame (WF) was then set on a clean surface and remnant distilled water was absorbed from the surface of the OD with the aid of low lint tissue. Contact with the window and the tissue was avoided and remnant water around the segment was drawn away by means of capillary action. The ODs were then set aside

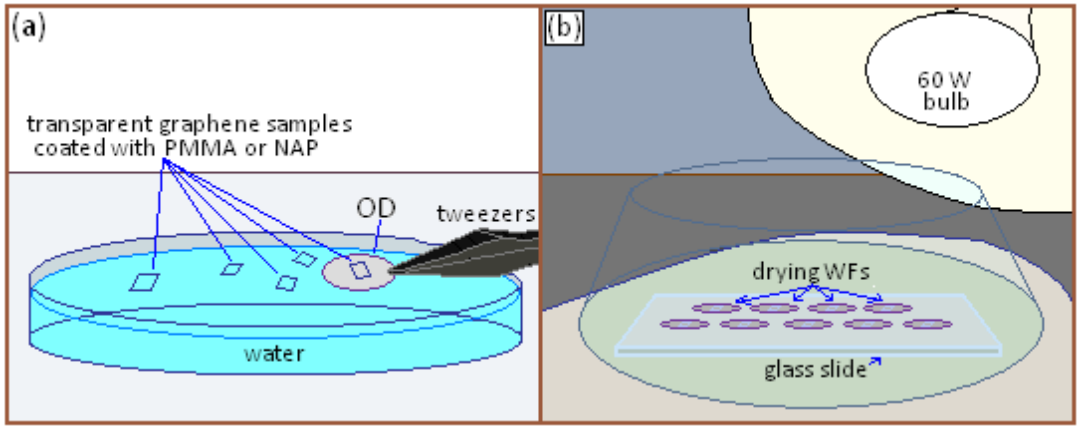

Figure 9. Deposition of the graphene/polymer segment onto the final OD substrate: (a) an OD was positioned under the floating segment while centering the segment above the flow orifice. The OD was then lifted vertically, depositing the segment over the orifice. After removing excess water, (b) the ODs were then placed on a clean microscope slide, which was covered with a glass bowl and then placed near a filament bulb to assist in removing residual water.

near a filament bulb (60 W) to dry completely with the heat of the bulb aiding the drying process (Figure 9 (b)).

2.3 Improving the Adhesion of the Graphene Layer to the Substrate of Interest

An additional heat treatment was then applied to the WFs containing the first type of protective layer, PMMA, in attempts to help achieve better interfacial contact between the graphene membrane and the OD on which it was suspended, following the protocol from reference [22]. The ODs were heated on a hot plate for time durations varying between 3 h to > 12 h at temperatures ranging between 150°-180° C. PMMA polymerized solely from methyl methacrylate monomers has a glass transition temperature (T_g) near 105° C [22]. Thus, the idea was to heat PMMA just above its T_g for an extended period of time so that the PMMA would lose rigidity and become flexible, allowing the graphene layer to fully settle onto the surface of the OD. With increased surface contact between the graphene membrane and the OD, the graphene membrane maintained greater adhesion to the microscopically rough substrate surface, thus better creating a seal between the sample environment and the vacuum imaging environment. The 'relaxed' WF was then ready for removal of the PMMA-type protective film.

2.4 Removal of the Polymer Support

The gentle removal of the polymer film from the graphene surface was a crucial task and is one of the limiting factors in fabrication of suspended graphene membranes. Removal of the protective layer was then approached by a tailored methodology dependent on the composition (PMMA vs. NAP) of the protective layer. Two different methods, namely a wet approach and a dry approach, were utilized to remove the

PMMA protective layer, while only the aforementioned wet approach was used for removal of the NAP protective layer.

2.4.1 Dry Approach

The first method utilized a dry approach through high-temperature flow-assisted evaporation of the protective PMMA layer with the vacuum-oven system shown in Figure 10. The WFs were placed in an alumina boat which was slid into the center of a quartz tube. The tube was placed into a Mini-Mite tube furnace with the alumina boat lying in the middle of the furnace's heating chamber. Vacuum flanges were attached to the ends of the quartz tube, with one flange connected to a primary input gas line and the other connected to a primary output gas line. Total flux along the primary input line was monitored with a floating ball flow meter connected to the primary input line leading directly to the input vacuum flange of the quartz tube. From the floating ball flow meter, the primary input line leads to a solenoid valve gating the total influx. After the solenoid valve, the input line branches into two separate lines, one ending at a needle valve connected to the regulator of a high-pressure hydrogen tank and the other leading to an Argon-rated flow meter, then terminating at the regulator of a high-pressure argon tank. Starting at the other vacuum flange, the primary output line leads

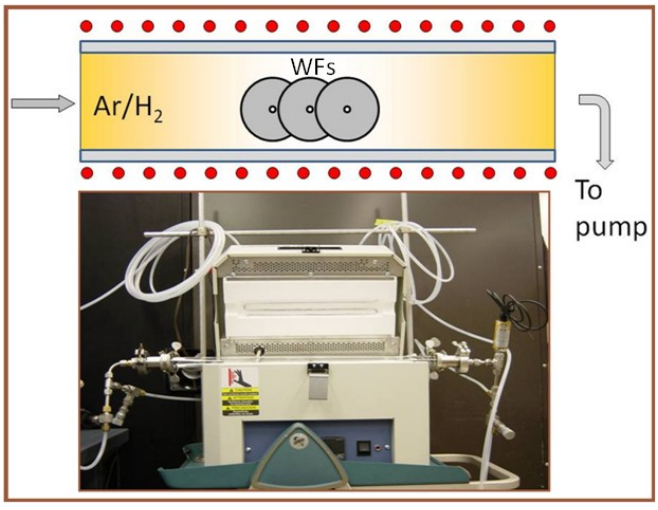

Figure 10. Medium Vacuum to Atmospheric Pressure Multi-component-gas-flow Furnace System: (top) the WFs were heated under a calibrated flow of Ar/H_2 for dry removal of the PMMA protective coating from the surface of the graphene membranes. (bottom) Shown here is the central furnace portion of the system.

to a needle valve, gating the total outflux from the quartz tube. From the needle valve, the primary output line then connects to a T joint gas line connector. At the T joint, the line branches into one line terminating at a roughing pump with the other connecting to a needle valve gating a line leading into a fume hood.

Following methods adopted from reference [22], the process of thermally removing the PMMA layer was initiated by first evacuating the quartz tube containing the WF to an absolute pressure in the range of 200-300 mTorr with a roughing pump. The input lines were then evacuated throughout their entire length up to the argon and hydrogen tank regulators down to an absolute pressure of ~300 mTorr. The needle valve gating the primary outflow line was then closed and hydrogen was promptly admitted into the primary input line until a pressure above 1 atm registered on the floating ball flow meter pressure gauge at the inlet of the quartz tube. The needle valve gating the output line to the fume hood was opened, followed by fully opening the needle valve gating the total outflux from the tube. With the quartz tube now flushed solely with hydrogen, the needle valve on the regulator for the hydrogen tank is adjusted to achieve a hydrogen influx of ~25-35 sccm on the floating ball flow meter. Argon was then admitted into the quartz tube at a flow rate which doubled in initial flow rate registering on the floating ball flow meter, thus achieving a gas influx composed of 50% hydrogen and 50% argon at nearly atmospheric pressure within the quartz tube. The tube furnace was then turned on with the heat ramped up to and maintained at 350° C for 2.5 hours. After the latter time duration, the furnace was switched off with the H_2/Ar flux maintained until the quartz tube reached a temperature below 100° C. With the

PMMA protective layer thermally removed, the WFs were removed from the quartz tube and now functional, ready to be assembled into the e-cell.

Argon gas was used as a component of the annealing flow mixture as a carrier gas to remove the evaporated PMMA from the annealing chamber but also as a dilutant for the other hydrogen gas component to inhibit combustion. Although oxygen has been shown to assist in the decomposition of PMMA at annealing temperatures [24], its presence also increases oxidation potential for the graphene membrane [15]. Thus, oxygen is omitted and instead solely hydrogen is included along with argon in the gas flow mixture. The flow of hydrogen is understood to also function as a carrier gas. More importantly though, hydrogen functions as a reducing gas, inhibiting further oxidation during PMMA decomposition primarily by reducing generated radicals as well as reducing surface oxidation already potentially present on the graphene membrane [2]. Annealing graphene at 300° C in an H_2/Ar directed flow has also been shown to improve graphene's Young's modulus and tensile strength. The annealing temperature was maintained higher at 350° C since full PMMA decomposition begins to occur near this temperature [13, 24]. Although slow PMMA decomposition can occur at temperatures around 165° C due to the breaking of H-H bonds, followed with the removal of end groups from the polymer chains as the temperature continues to increase beyond 270° C, the energy needed to break the carbon-carbons bonds within the backbone of the polymer chain is not sufficient until the oven reaches the target annealing temperature [13, 24].

Residual networks of PMMA with possible remnant metal oxides from the growth substrate were most likely present on the annealed graphene, regardless of the

annealing time and cannot even be removed at high temperatures when graphene begins to decompose [15]. The primary mechanism behind this is most likely due to macroradicals, or free radical macromolecules, forming from the decomposing bulk PMMA which covalently bond to the higher energy grain boundaries and defect sites of the graphene sheet, since only lower binding energy physisorption can occur between pure graphene and the macroradicals. The macroradicals bonded to the defect sites on graphene also can be attached to other heavy molecular fragments, which could influence surrounding polymer chains, inhibiting their removal at high temperatures as well. Although neither wet methods using organic solvents or high temperature annealing can remove the residual networks of PMMA, the thickness of the remnant networks will primarily correspond to a single layer of PMMA, thus not substantially distorting images or spectra but rather inherent as unwanted low-level noise.

2.4.2 Wet Approach

Organic solvents were utilized in wet removal method used to remove both PMMA and NAP. To reduce the probability of graphene membrane disruption by the capillary forces, solvents with reduced surface tension coefficients were used. The approach utilized two containers of acetone heated near the boiling point to both enhance the solvent's reactivity and reduce its surface tension. In addition, this prevented water condensation on the orifice due to fast evaporative cooling of the solvent. The containers were set on a hot plate maintaining a temperature of 55° C. The two containers of acetone, defined as primary and secondary acetone, were contained in a 5 cm diameter Pyrex® petri dish and 30 ml Pyrex® beaker, respectively. To begin removal of the protective layer, the WF was held with its plane parallel to the

surface of the primary acetone membrane-side-up and placed in the vapors directly above the primary acetone for ~5 min, during which the protective layer on the membrane would lose its rigidity and relax (Figure 11 (a)). As the protective layer of the membrane softened, the surface contact would increase between the membrane and primary frame, allowing for greater adhesion capabilities from van der Waals interactions which ultimately provided the adherence between the graphene layer and the primary frame. Any remaining visible wrinkles in the membrane or gaps present between the membrane and the primary frame in proximity of the orifice could be smoothed out carefully at this state if necessary by manipulating the membrane's edge with tweezers. Once the membrane had been allowed to fully relax and maximum surface contact between the graphene multilayer and the primary frame was achieved, the WF was tilted 90° so as to make its plane perpendicular to the surface of the acetone and slowly submerged at a rate of ~0.3 mm/s (Figure 11 (b)). The WF was held fully submerged for a duration of 5-10 min in hot acetone, allowing the protective layer on the graphene membrane to fully dissolve in the solvent. The WF was slowly pulled out of the primary acetone, maintaining its orientation and then slowly submerged (~0.3 mm/s) in the secondary acetone, again with its plane perpendicular to the surface

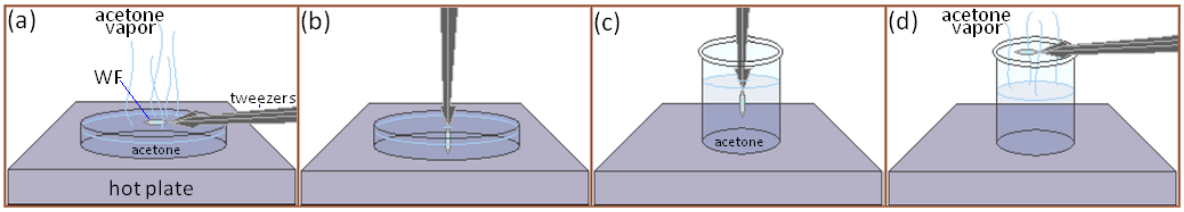

Figure 11. The wet approach to PMMA and NAP removal from graphene: (a) the WF was held in the vapors of the heated acetone, and then (b) dipped into the primary acetone solution, dissolving the PMMA or NAP layer. The WF was then removed from the primary acetone, and then (c) submerged a final time in the secondary acetone. (d) When removing the WF from the secondary acetone, it was held just below the rim of the beaker to dry so as to inhibit atmospheric water from condensing on the WF.

of the acetone (Figure 11 (c)). The WF was held fully submerged for 5-10 min, and then slowly removed from the acetone yet held just below the beaker's rim in the acetone vapor until the acetone had fully evaporated from the surface of the WF without any condensation of atmospheric water (Figure 11 (d)). The WF was then fully removed from the beaker and then safely stored, ready for assembly into the e-cell body.

2.5 Avoiding Mechanical Distortion of the Suspended Membrane due to the Geometry of the Orifice

Usually in the process of laser drilling the 3-10 micron diameter orifices in the ODs, small 'lips' and melted metal micro-droplets would be found created at the perimeter of the entrance/exit of the orifice (Figure 12 (a), (b)). These sharp features, inducing strong local tension on the graphene membrane promoted disruption of the membrane. The high aspect ratio of the micron-size channel through the OD also created favorable conditions for the orifice to often become clogged. To address these issues, an electrochemical polishing (EP) cell was built to both

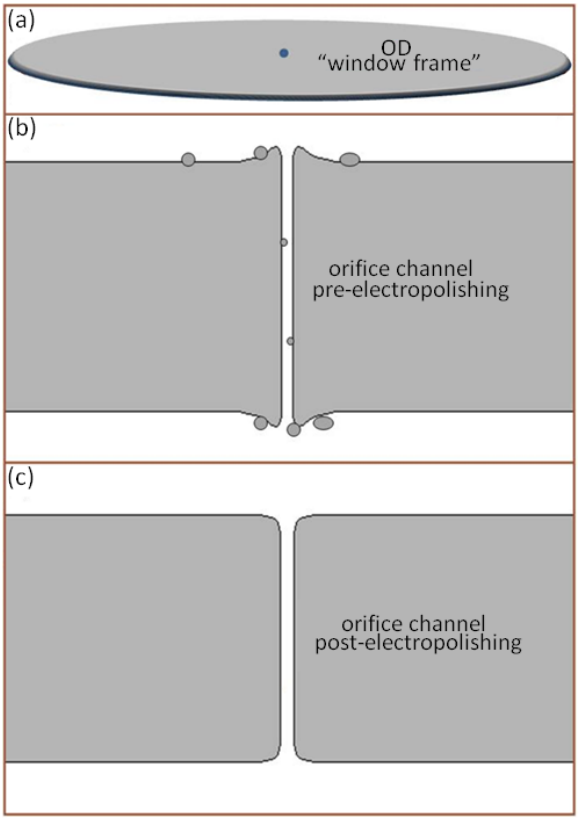

Figure 12. Prior to membrane deposition, (a) the as-received flow orifice disc required initial structural processing. (b) "Lips" near the openings of the micro-channel and metal micro-droplets were obstructive features remnant from the laser drilling procedure. (c) After the electropolishing procedure, obstructive particulates were removed and the perimeters at the inlets to the microchannel became rounded.

initially process the ODs, and to later clean their surfaces and unclog the orifice once vacuum tests or imaging for the WF was complete. Prior to membrane deposition, as arrived ODs were polished until the edges of the exit/entrance of the orifice became rounded (Figure 12 (c)). When EP an object, high surface area features such as points and edges are dissolved at a higher rate since dissolution occurs at the interface of the solution and the surface of the object. Thus, the smooth surface and rounded edges of the orifice entrance/exit allowed for higher surface area contact between the OD and deposited graphene membrane, promoting optimum van der Waals adhesive forces at the their interface and discouraging membrane rupture from fine edges or points at the orifice perimeter.

The EP cell (Figure 13) contained ~20 ml of a solution consisting of 45% phosphoric acid, 30% sulfuric acid, and 25% glycerol by volume. The solution was housed in a Pyrex® beaker and capped with a rubber stopper which had two holes through which two threaded rods were passed to serve as positive and negative terminals for supplying current through the solution. The positive terminal made electrical contact with three screws which served to clamp and hold the ODs (anode) while submerged in the electropolishing solution. Similarly, the negative terminal maintained electrical contact between three screws which held a ~1x2 cm^2 sheet of stainless steel (cathode) submerged in the solution, with a ~1.5 cm gap between the anode and cathode. A small magnetic

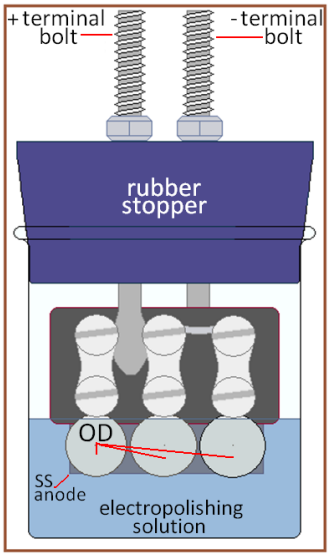

Figure 13. The electropolishing cell: three ODs are held submerged in the electrolytic solution.

stir rod was placed within the solution to facilitate polishing by driving homogeneity within the solution from dispersing local ionic and molecular concentrations near the electrodes. A power supply was connected to the threaded electrodes, maintaining a voltage of 4 V and supplying a current of roughly 0.4 A per OD, thus providing a constant current density of ~4 mA/cm^2 regardless of the number of ODs clamped in to the apparatus. The EP cell rested on a hot plate preheated to ~45° C, which was responsible for driving the magnetic stir rod.

When fully assembled and preheated, the power supply was switched on for 30 s and then turned off, completing the polishing procedure. The polished ODs, still clamped in the apparatus, were removed from the electropolishing solution and the electrode assembly was briefly submerged in distilled water. The ODs were then removed from the electrode assembly and sonicated for 5 min in distilled water individually to avoid unwanted high-energy collisions between multiple ODs which could generate micro-fragments of stainless steel which could potentially clog the orifice. The ODs were then placed individually in beakers containing acetone and heated to acetone's boiling point on a hot plate. Once the appropriate temperature was reached, the ODs were promptly sonicated in the acetone for another 5 min. At this point, with the ODs fully polished and cleaned, they were removed from the acetone with tweezers. Any acetone remnant on the OD and at the tweezers/OD interface was drawn through capillary action by gently dabbing the perimeter of the OD and near the tips of the tweezers with LDTP, thus discouraging any coffee ring effects which would have otherwise fostered the formation of organic residues in and at the proximity of the orifice. To verify that the orifice was not blocked by debris, the ODs were inspected

under an optical microscope, verifying clearance (blockage) of the orifice when transmitted light was visible (not visible) through the orifice. ODs still clogged after the electropolishing procedure were treated with a second heating in acetone and an additional five minutes of sonication, removing remnant acetone in the same manner as described previously.

Alternatively, oxygen plasma cleaning was attempted to remove organic residues or unwanted graphene layers. However, due to lack of establishing an ability to control the radically enhanced oxidation at elevated temperatures, this method was omitted.

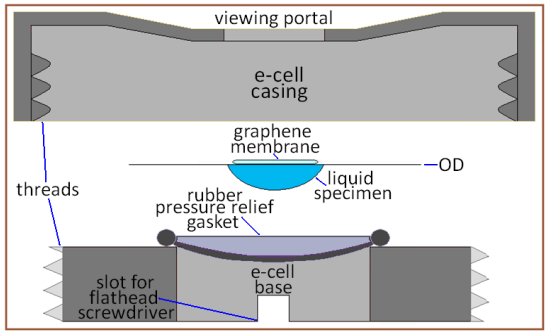

Figure 14. A cross-sectional view of the e-cell: with the base and casing being threaded, the cell is assembled in the vertical order shown above, and the base is screwed into the casing by means of a flathead screwdriver driving the base. The base contains a membrane gasket which provides pressure relief due to its elasticity, as well as functioning to create the inner walls of the sealed environment by creating a cavity between the bottom face of the WF and the membrane gasket. The top casing contains a viewing portal, under which the membrane covered orifice is to be centered. For testing SEM imaging capabilities with the e-cell, the under-side of the orifice was covered with a droplet from a water solution containing 50 nm Au NP to serve as the imaging specimens.

2.6 Design of the Environmental Cell

The e-cell body was fabricated from stainless steel from a simple design allowing for quick and easy placement of the WF and the sample to be imaged (Figure 14). The e-cell is cylindrical with an assembled height and diameter of 4.75 mm and 17 mm, respectively. The base of the e-cell contains a rubber gasket membrane centered over a hole in the e-cell base, serving as an expanding wall of the sample environment for pressure relief during imaging under vacuum. The center-slotted bottom-side of the base allows for a flat-head screwdriver to drive the base into the casing, of which the

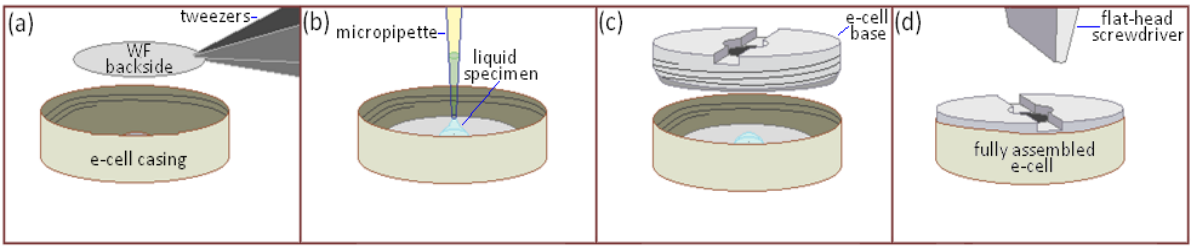

Figure 15. To assemble the e-cell, (a) the WF was placed in the top casing of the cell with the side containing the graphene membrane facing down and the orifice centered above the viewing portal within the top casing. (b) A droplet of the solution to be imaged was drop-cast over the orifice. (c) The base was then inserted into the top casing and (d) screwed in with a flathead screwdriver.

inside walls are also threaded. The top face of the casing contains a small 2 mm hole, allowing exposure of the graphene membrane containing side of the WF to the outer environment. To assemble the e-cell for imaging, the WF was first placed in the top casing of the e-cell (Figure 15 (a)), aligning the g-membrane with the e-cell's viewing hole. For an imaging sample, 20 μl from one of two solutions of 50 nm colloidal gold (Ted Pella) and distilled water (1:1 and 5:1, Au:H_20) was delivered via micropipette to the center of the WF's blank side over the orifice (Figure 15 (b)) and the e-cell base was inserted into the casing (Figure 15 (c)) and tightened with a screwdriver (Figure 15 (d)). As the base entered the casing, the gasket compressed against the sample-containing face of the WF and sealed in the sample between this face and the rubber gasket membrane. This volume between the WF and the rubber gasket membrane functioned as the cell's environment. With the e-cell casing, base, and WF all being composed of stainless steel, any charge-accumulation induced by imaging would be alleviated when the cell base was grounded. Once imaging was complete, the e-cell was dissembled and the used WF could be simply replaced with a new, pristine WF.

2.7 Vacuum Compliance Tests

Vacuum tests were conducted on the WF before SEM imaging to ensure the membrane provided an adequate seal over the orifice of the OD "frame", as tears may

have been present in the membrane or adequate adhesion between the membrane and OD may not have been established. A small, windowed vacuum chamber was constructed and driven by a roughing pump to simulate medium vacuum conditions (Figure 16). A thermocouple pressure gauge was connected to the vacuum chamber to measure its internal pressure and a needle valve on the side of the chamber venting to atmosphere allowed for a slow and controlled reduction of the internal pressure down to vacuum conditions. For vacuum testing, a 5 μL drop of distilled water was deposited over orifice on the membrane-free face of the OD after the WF was placed into the e-cell (Figure 15 (a), (b)). The e-cell was then assembled (Figure 15 (c), (d)) and placed on an elevated pedestal containing a layer of dual-sided carbon tape to maintain the e-cell's position. The top, windowed vacuum flange was attached and tightened to the chamber body and the entire assembly was placed under a stereomicroscope with the windowed flange and contained e-cell's viewing portal centered in the microscope's viewing area and focused on the membrane-capped orifice (Figure 16). With the needle-valve fully opened, the roughing pump was

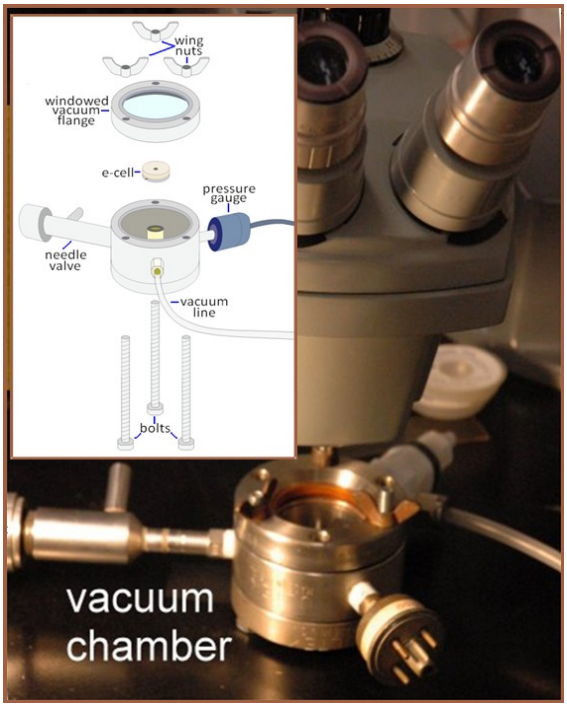

Figure 16. The vacuum chamber used for preliminary vacuum testing of the WF: (main) the vacuum chamber's window centered under the viewing area of a stereomicroscope used to observe the orifice during vacuum testing. (inset) The disassembled vacuum chamber is shown. A pressure gauge and needle valve are attached to the volume of the chamber, which is evacuated by a roughing pump attached to a nylon gas line joining the former and the latter.

switched on and the orifice was carefully observed through the microscope. Due to the water placed over the orifice on the now opposing side of the WF, any leaks from the cell's environment through the orifice into the vacuum chamber could be observed with the passage of water ejecting or bubbling up through the orifice. The needle valve was slowly closed completely while still observing the membrane-capped orifice until a minimum pressure of 550 mTorr was reached. If no water was observed bubbling or ejecting through the orifice and no obvious membrane disruption had occurred, the needle valve was again opened, bringing the volume of the vacuum chamber back to atmospheric pressure. After removing the e-cell from the vacuum chamber, it was dissembled and the WF, having passed the vacuum test was safely stored away for ESEM model testing.

2.8 SEM Imaging Parameters

A Hitachi 4500 SEM utilizing a field emission gun as an electron source was used for observing detailed features of the WF in the region of the orifice visible through the e-cell viewing portal. For topological analysis of the membrane's surface and the orifice perimeter, a PE beam energy of 2-4 keV was used in conjunction with upper and lower SE detectors (SEDs) for image formation. For imaging deep through the membrane, a 20 keV PE beam energy was used with electron detection for image formation achieved by a BSED. One of two of the 50 nm colloidal Au water mixtures mentioned previously in the section, *Design of the Environmental Cell,* was dropcasted on the environmentally contained side of the graphene membrane for use as model objects to test imaging parameters. Due to the high Z-number of Au, an optimal Z-contrast was achieved, providing greater differentiation in the final image between the

modeled object and liquid suspending solution, this being due to Au's effectively large resultant BSE responding image signal relative to that of water's.

CHAPTER 3

RESULTS AND DISCUSSION

3.1 Electrochemical Polishing Results

The effects of brief EP on the surface features at the inlet to the orifice within the OD can be observed below in Figure 17, with the images on the left and right corresponding to pre- and post-initial EP treatment. The level of roughness and presence of jagged edges is quite high on the perimeter of the orifice pre-EP, whereas the perimeter of the orifice post-EP has become smooth, lacking the fine surface details originally present on the former orifice perimeter. Since EP removes the SS304 material by means of field enhanced etching, high profile features are first removed, followed by a generally uniform removal of the bulk. Due to the latter means of EP

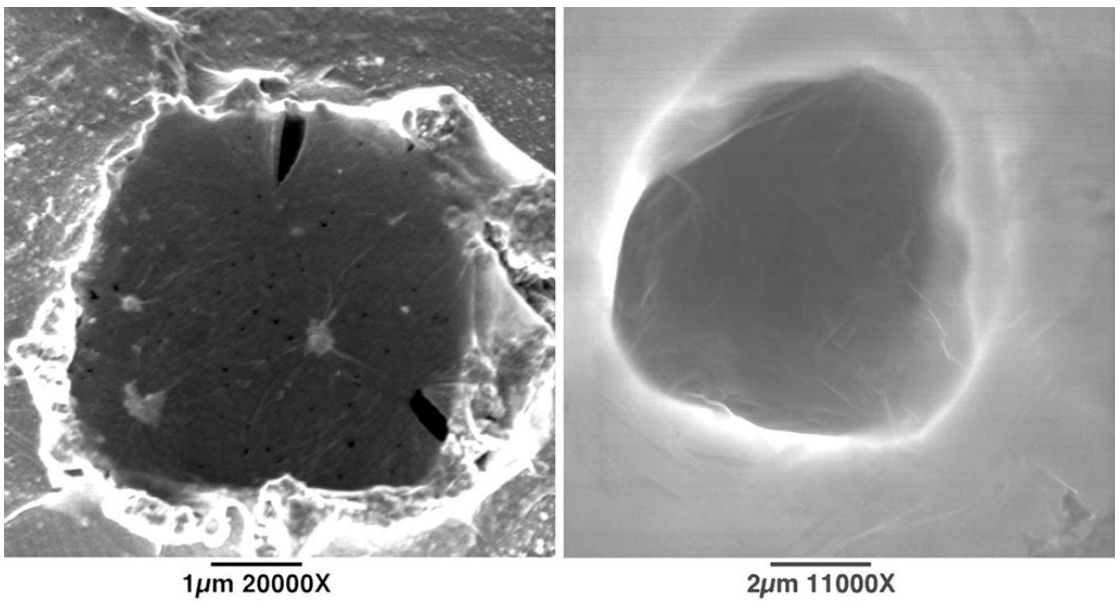

Figure 17. SEM images of the orifices within the ODs pre- (left) and post- (right) initial EP treatment: (left) the ~4.1 μm inner diameter at the surface of the inlet exhibits a jagged texture, with fine surface details and metal micro-droplets visible in the extremities of the image beyond the orifice perimeter. (right) The same orifice post-initial EP treatment, now ≈ 6.8 μm diameter and with smooth, rounded edges at the perimeter of the inlet to the orifice. A few minor surface details can be distinguished beyond the inlet perimeter.

action, the orifice inlet diameter can be increased by about 60% post-EP. The outline of the orifice inlet diameter post-initial EP is faintly visible as the outermost edge of the jagged orifice inlet perimeter in the image of the orifice pre-initial EP displayed in the left image within Figure 17.

With its surface modified, the OD subjected to EP treatment becomes more hospitable to a tear-free suspension with an increased adhesion of deposited graphene membranes due the EP's removal of sharp features and the resultant increase in surface area contact between the OD and the deposited graphene membrane. This translates to achieving a higher quality membrane with an increased mechanical robustness for withstanding forces at the differential pressure interface present on either side of the graphene membrane within the WF of the e-cell during imaging in the evacuated SEM specimen chamber. The increased diameter and surface smoothness at the inlet to the orifice also lowers the potential for the orifice to become clogged, aiding in subsequent cleaning of contaminated ODs, though this is a slight trade-off since as mentioned previously the probability for the membrane to survive tends to be inversely related to the orifice diameter.

3.2 Dry vs. Wet Removal of PMMA

The approached removal methods for PMMA yielded similar final results, as partially evident in observance of the SEM images shown in Figure 18, which reveal remnant films of PMMA that still cover the majority of the graphene membrane's surface that will ultimately exist as image distortion and increase the minimum PE beam energy requirement for achieving sufficient imaging contrasts with BSE detection and lower the

likelihood for an adequate collection of weak SE emission from the specimens underlying the PMMA/graphene.

The dispersion of the remnant PMMA differs for both removal approaches, which is generally homogenous over the graphene surface with a few PMMA-free islands and a few strips of thicker remnant PMMA for the dry removal approach. The wet-removal method also yielded nearly full surface coverage from remnant PMMA, yet there existed a smaller divergence of its thickness gradient over the surface, thus there were larger PMMA-free islands with surface layer PMMA borders that would more gradually vary in thickness over the surface of the graphene membrane. This variance in remnant PMMA between the two approaches results in a roughly consistent image distortion for specimens viewed under graphene membranes produced by the dry removal approach and a more steadily varying image distortion with > 1 μm^2 PMMA-free regions for

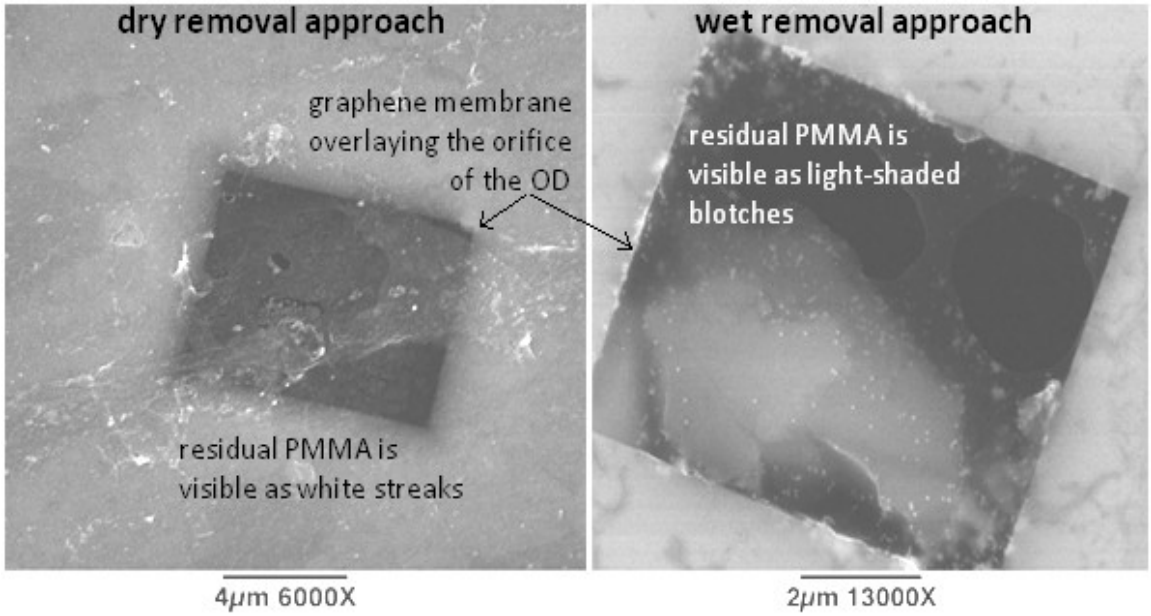

Figure 18. SEM images of graphene membranes overlaying the viewing orifice within the e-cell, showing typical dispersion of remnant PMMA after 12 hours of annealing at 170° C subsequent to using the (left) dry and (right) wet PMMA removal methods. Neither removal method could effectively clean the graphene surface. Although image distortion differs in quality between the two methods, the overall quantity of distortion is roughly the same, thus neither PMMA removal approach was deemed preferable.

graphene membranes produced with the wet removal approach.

Both approaches also yielded final WFs which contained cracks and micro-holes while lacking any differentiable rate of occurrence between the two approaches, thus it is possible these defects were created in WF synthesis steps not specific to PMMA removal. Thus, for efficiency in time and energy whilst using the least and minimally expensive equipment, the wet removal approach is deemed optimal among the two PMMA removal methods approached. In addition to the latter conclusions concerning the application and clean removal of the protective layer utilized for graphene isolation from its respective substrate, the NAP protective polymer was not observed to produce final results which differed significantly from those utilizing PMMA in the wet approach.

3.3 Imaging in the Liquid Phase

The effectiveness of the graphene membrane as an electron transparent window whilst maintaining structural stability under high vacuum conditions is evident from the SEM images in Figure 19. Using a 20 keV PE beam energy, the membrane appears fully transparent using the BSED to image the specimen volume (Figure 19(a)). Upon further increasing magnification, the membrane and contained Au NP colloidal in water both in the vicinity of the membrane and adhered to its enclosed surface became visible using a SED (Figure 19 (b)). Using the BSED at the same magnification, the Au NP contrast significantly improves due to the membrane being transparent to the higher energy PEs and BSEs (Figure 19 (c)).

Relative to the energy of emitted SEs, higher energy BSEs resulting from PEs travelling through the membrane and elastically scattering upon colliding with the heavy nuclei of imaged specimens are of adequate energies to be transmitted back through

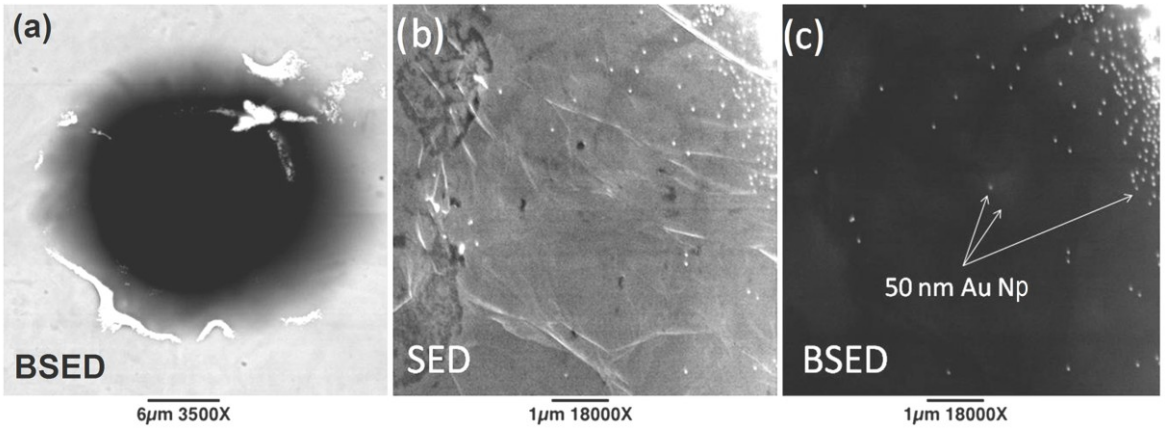

Figure 19. SEM images of the membrane capped-orifice within in the e-cell, produced with a 20 keV PE beam and with 50 nm Au NP dispersed in water lying on the enclosed side of the graphene membrane: (a) using the BSED for image formation, the volume of the orifice is visible, seen as the black region due to the low Z-number of both the water and the membrane relative to that of the SS OD. (b) Upon increasing the magnification and using the SED, topological features of the membrane and Au NP near the enclosed surface of the membrane became visible. (c) When switching to the BSED without modifying the degree of magnification, all features associated with the graphene membrane became transparent to the higher energy electrons whilst producing negligible backscattering effects, thus rendering the contained Au NP highly visible due to the high degree of contrast that could be obtained from the high Z-numbered Au NP.

the membrane, the latter being a result of graphene's relatively large λ_{IMPF} of electrons at low electron energies. Since the brightness of the specimen is dependent on the probability for electron backscattering to occur, contrast is created by chemical variation due to the proton density, or the atomic-number (Z-number) arising from the elemental composition of the specimen. With a Z-number of 6, carbon produces negligible electron backscattering effects relative to the Au NP, with water being relatively transparent as well due to similar reasoning. The Au NP are highly responsive to the PE beam in producing electron backscattering effects, evident in the high rate of BSE generation due to gold's significantly higher Z-number of 79. The PMMA and NAP, both of which are primarily composed of low Z-number elements (the cured NAP consists primarily of nitrocellulose [5]) became highly transparent as well at the 20 keV imaging conditions using the BSED.

Lower energy SE emission arises from inelastic scattering interactions between the PE beam and the membrane/specimen. Due to the lower energy of the SEs, these electrons usually provide a topological image, yet the Au NPs were still visible behind the membrane.

3.4 Parasitic Effects and Limiting Factors

Due to intrinsic phenomena arising when irradiating liquid water with high energy electrons, additional molecules and reactive radicals made of hydrogen and oxygen were formed due to water radiolysis when SEM imaging colloidal Au NP in water. We observed the formation of bubbles, accumulating at the backside of the graphene membrane (Figure 20). The bubbles were observed to form as a result of zooming in on the water region beneath the membrane due to the resulting increase of the PE spatial density within the latter region. Upon the formation of bubbles presumed to be

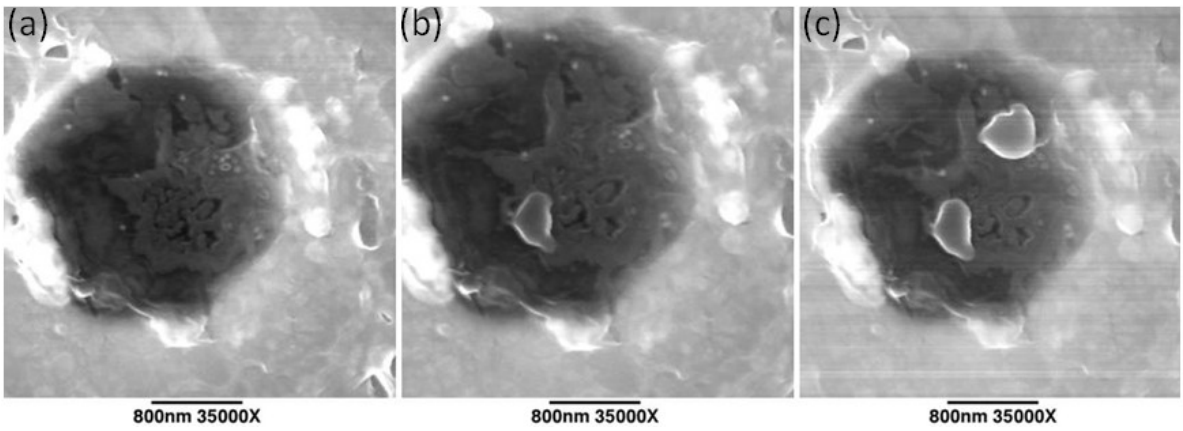

Figure 20. Observed bubble formation when using the e-cell for SEM imaging Au NP dispersed in water due to water radiolysis: (a) the first image of the ~3 micron diameter orifice reveals solely a few Au NP visible beneath the graphene membrane. (b) Within the second image, a bubble is visible, assumed to be H_2 forming due to the PE beam interacting with the water, having formed due to zooming in on the respective area [26, 34]. (c) Upon taking a third image, the first bubble has increased slightly in size and another bubble has formed at the undersurface of the graphene membrane, again forming due to the increased concentrated PE dosage resultant from zooming-in on that region. As seen above, the bubbles can obscure imaging, while the resulting increase in pressure within the e-cell due to the liquid to vapor phase transition encourages membrane disruption by increasing the pressure differential to be maintained solely by the van der Waals interactions between the areas of the membrane in surface contact with the OD.

composed primarily of H_2 with a small fraction of O_2, the pressure would increase within the e-cell, thus promoting disruption of the membrane due to the increased pressure differential at the membrane interface [11, 26, 35]. The H_2/O_2 vapors form from various ionic and molecular intermediate reaction steps upon water ionization, dissociation, and recombination processes occurring in response to the PE beam interacting with water in the e-cell. Taking into consideration the density variations solely for water in the imaged specimen arising from liquid to vapor phase transitions at ~STP, every molecular unit of H_2 and O_2 gas produced by water radiolysis from the PE beam occupies roughly 10^4 and 10^3 times greater volume, respectively, than the water molecules in liquid phase.

Variables primarily responsible for H_2 vapor production have been identified since a limiting dosage was not found to have been definitively reported in scientific literature. The variables' proportionalities to the molecular generation rate of H_2 per second during SEM imaging of water in an e-cell are defined in the following:

$$M_{H_2} \propto E_{PE} \times FR_{PE\ Beam} \times (1/r_{PE\ Beam})^2 \times (1 - BSC_{Mean}) \times G_{H_2} ,$$

where a constant BSC of 0.05 for water behind a 3 monolayer graphene membrane (from Casino simulations [12]) and a generation rate of 1.5 H_2 gas molecules per 100 eV of energy absorbed by the water from PE beam interactions can be assumed for quantitative comprehension [26]. The first three variables on the right side of the above proportionality correspond to those which the SEM operator can influence; therefore, these should be considered when trying to manage the vapor generation phenomenon. Table 3 defines the variables expressed in the latter proportionality.

All variables strongly influencing water radiolysis, such as the PE beam energy, PE intensity, scanning rate, total energy absorption [17], PE beam interaction volume

[31], total volume of water contained in the e-cell specimen containment volume [34], along with specimen and peripheral orifice features which inhibit charge/solution equilibration [19, 30] balance the total generation of H_2/O_2 vapor production. Water radiolysis is an inescapable phenomenon arising in the high energy and high spatial-density electron bombardment of hydrated specimen, but by addressing key variables which are primarily responsible for driving this mechanism, the limiting effects encountered when SEM imaging water specimens with the e-cell can be minimized.

Table 3
Variables expressed in the molecular generation rate proportionality for hydrogen gas per second (M_{H2}) due to water radiolysis

Variable	Variable's Representation
M_{H2}	molecules of H_2 generated per second
E_{PE}	energy of the PE beam
$FR_{PE\ Beam}$	firing rate of the PE beam
$r_{PE\ Beam}$	radius of the PE beam incident on the water specimen
BSC_{Mean}	membrane/specimen cummulative mean BSC
$G(H_2)$	generation rate of H_2 (molecules/100 eV)

CHAPTER 4

CONCLUSION

We developed and tested a simple methodology for transferring 1-4 monolayer graphene from Cu/Ni foil and Ni/SiO_2/Si substrates onto the final SS ODs, whilst incorporating an initial mechanical processing of the as-received ODs for greater membrane stability and adherence. Included with this, methods for restoring used WFs back to clean ODs for re-use were founded. The potential of the in-lab developed e-cell, with its capability for using replaceable WFs for re-use within the main cell body is comparable to current commercially available QuantomiX cells with a theoretically extended minimum threshold in the lower PE beam energies for obtaining sufficient imaging contrasts through a three monolayer graphene membrane.

We tested the e-cell design for its ability to maintain membrane integrity in the high vacuum conditions of the SEM imaging chamber whilst surviving the PE beam irradiation, becoming nominally opaque to minimally energetic electrons relative to alternative membrane materials such as the 50 nm Si_3N_4 and the 150 nm Kapton polyimide membranes.

The e-cell's ability to allow imaging of a three phase system was verified and with it we were able to image 50 nm Au NPs in colloidal suspensions in liquids as model samples whilst observing the third phase vapor production of H_2/O_2 generated by SEM induced water radiolysis resultant primarily from specimen/PE interactions. The Au NPs were observed through the membrane using both a BSED and a SED, verifying its use for both electron microscopy and spectroscopy.

The parasitic effects of water radiolysis at high electron doses were supported by simple theoretical considerations. In defining limitations of the e-cell technology, the lack of any discernible preference in the outcomes of the two protective layers and two removal approaches was concluded with all variations to the layer types and removal approaches founded to be leaving remnant residue on the applied face of the graphene membrane. The latter limitation is symptomatically founded in the imaging capability, most markedly in its hindrance of stimulated SE emission by the specimen and subsequent detection by the SED while slightly increasing the PE beam energy requirement for imaging now through both the membrane and the residue layer.

To conclude: the proposed methodology is the next step forward in the development of high yield production protocols for electron ultra-transparent windows utilized for in situ / in vivo microscopy and spectroscopy of specimen in their native environment.

REFERENCES

[1] Abrams, I. M., & McBain, J. W. (1944). A CLOSED CELL FOR ELECTRON MICROSCOPY. *Science (New York, N.Y.), 100*(2595), 273-274. doi: 10.1126/science.100.2595.273

[2] Behar, V., Nechushtan, A., Kliger, Y., Gileadi, O., Sprinzak, D., Zik, O., & Karni, Y. (2007).

[3] Bhaviripudi, S., Jia, X. T., Dresselhaus, M. S., & Kong, J. (2010). Role of Kinetic Factors in Chemical Vapor Deposition Synthesis of Uniform Large Area Graphene Using Copper Catalyst. [Article]. *Nano Letters, 10*(10), 4128-4133. doi: 10.1021/nl102355o

[4] Booth, T. J., Blake, P., Nair, R. R., Jiang, D., Hill, E. W., Bangert, U., . . . Geim, A. K. (2008). Macroscopic graphene membranes and their extraordinary stiffness. *Nano Letters, 8*(8), 2442-2446. doi: 10.1021/nl801412y

[5] Castelain, M., Veyrat, S., Laine, G., & Montsatier, C. (1997). Contact dermatitis from nitrocellulose in a nail varnish. [Article]. *Contact Dermatitis, 36*(5), 266-267. doi: 10.1111/j.1600-0536.1997.tb00217.x

[6] Champion, Y., Bernard, F., Millot, N., & Perriat, P. (2005). Surface adsorption effects on the lattice expansion of copper nanocrystals. *Applied Physics Letters, 86*(23). doi: 10.1063/1.1947887

[7] Chang, Q. H., Huang, L., Ji, L. C., Wang, T., Ling, B., & Yang, H. F. (2010). Few-layer graphene direct deposition on Ni and Cu foil by cold-wall chemical vapor deposition. *Proceedings 8th International Vacuum Electron Sources Conference and Nanocarbon (2010 IVESC)*. doi: 10.1109/ivesc.2010.5644264

[8] Cohen, O., Beery, R., Levit, S., Ilany, J., Schwartz, I., Shabtai, M., . . . Karasik, A. (2006). Scanning electron microscopy of thyroid cells under fully hydrated conditions - A novel technique for a seasoned procedure: A brief observation. [Article]. *Thyroid, 16*(10), 997-1001. doi: 10.1089/thy.2006.16.997

[9] Danilatos, G. D. (1988). FOUNDATIONS OF ENVIRONMENTAL SCANNING ELECTRON-MICROSCOPY. [Review]. *Advances in Electronics and Electron Physics, 71*, 109-250.

[10] Daulton, T. L., Little, B. J., Lowe, K., & Jones-Meehan, J. (2001). In situ environmental cell-transmission electron microscopy study of microbial reduction of chromium(VI) using electron energy loss spectroscopy. *Microscopy and Microanalysis, 7*(6), 470-485.

[11] Dewhurst, H. A., Samuel, A. H., & Magee, J. L. (1954). A theoretical survey of the radiation chemistry of water and aqueous solutions. *Radiation research, 1*(1), 62-84. doi: 10.2307/3570180

[12] Drouin, D., Couture, A. R., Gauvin, R., Hovington, P., Horny, P., Demers, H., . . . Poirier-Demers, N. (2011). CASINO (Version 2.48). Universite de Sherbrooke, Sherbrooke, Quebec, Canada.

[13] Ferriol, M., Gentilhomme, A., Cochez, M., Oget, N., & Mieloszynski, J. L. (2003). Thermal degradation of poly(methyl methacrylate) (PMMA): modelling of DTG and TG curves. *Polymer Degradation and Stability, 79*(2), 271-281. doi: 10.1016/s0141-3910(02)00291-4

[14] Gries, W. H. (1996). A universal predictive equation for the inelastic mean free pathlengths of x-ray photoelectrons and Auger electrons. *Surface and Interface*

Analysis, 24(1), 38-50. doi: 10.1002/(sici)1096-9918(199601)24:1<38::aid-sia84>3.3.co;2-8

[15] Hovmoller, S., & Zou, X. D. (2011). Introduction to electron crystallography. [Editorial Material]. *Crystal Research and Technology, 46*(6), 535-541. doi: 10.1002/crat.201000531

[16] Huang, L., Chang, Q. H., Guo, G. L., Liu, Y., Xie, Y. Q., Wang, T., . . . Yang, H. F. (2012). Synthesis of high-quality graphene films on nickel foils by rapid thermal chemical vapor deposition. *Carbon, 50*(2), 551-556. doi: 10.1016/j.carbon.2011.09.012

[17] Jafarov, Y. D. (2011). MATHEMATICAL MODELING OF RADIOLYSIS PROCESS OF WATER UNDER THE IMPACT OF LOW-ENERGY ELECTRONS. [Article]. *Problems of Atomic Science and Technology*(5), 42-47.

[18] Joy, D. C., & Joy, C. S. (2006). Scanning electron microscope imaging in liquids - some data on electron interactions in water. *Journal of Microscopy-Oxford, 221*, 84-88. doi: 10.1111/j.1365-2818.2006.01548.x

[19] Kaplan, I. G., & Sukhonosov, V. Y. (1991). SIMULATION OF THE PASSAGE OF FAST ELECTRONS AND THE EARLY STAGE OF WATER RADIOLYSIS BY THE MONTE-CARLO METHOD. [Article]. *Radiation research, 127*(1), 1-10. doi: 10.2307/3578081

[20] Kolmakov, A., Dikin, D. A., Cote, L. J., Huang, J., Abyaneh, M. K., Amati, M., . . . Kiskinova, M. (2011). Graphene oxide windows for in situ environmental cell photoelectron spectroscopy. *Nature Nanotechnology, 6*(10), 651-657. doi: 10.1038/nnano.2011.130

[21] Krueger, M., Berg, S., Stone, D. A., Strelcov, E., Dikin, D. A., Kim, J., . . . Kolmakov, A. (2011). Drop-Casted Self-Assembling Graphene Oxide Membranes for Scanning Electron Microscopy on Wet and Dense Gaseous Samples. *Acs Nano, 5*(12), 10047-10054. doi: 10.1021/nn204287g

[22] Kumar, S., Adams, W. W., & Helminiak, T. E. (1988). UNIAXIAL COMPRESSIVE STRENGTH OF HIGH MODULUS FIBERS FOR COMPOSITES. [Article]. *Journal of Reinforced Plastics and Composites, 7*(2), 108-119. doi: 10.1177/073168448800700201

[23] Kumar, S., McEvoy, N., Kim, H.-Y., Lee, K., Peltekis, N., Rezvani, E., . . . Duesberg, G. S. (2011). CVD growth and processing of graphene for electronic applications. *Physica Status Solidi B-Basic Solid State Physics, 248*(11), 2604-2608. doi: 10.1002/pssb.201100179

[24] Lesiak, B., Jablonski, A., Prussak, Z., & Mrozek, P. (1989). EXPERIMENTAL-DETERMINATION OF THE INELASTIC MEAN FREE-PATH OF ELECTRONS IN SOLIDS. *Surface Science, 223*(1-2), 213-232. doi: 10.1016/0039-6028(89)90735-8

[25] Li, Y. L., Liang, Y., Zheng, F., Ma, X. F., & Cui, S. J. (2000). Sintering of nanopowders of amorphous silicon nitride under ultrahigh pressure. [Article]. *Journal of Materials Research, 15*(4), 988-994. doi: 10.1557/jmr.2000.0141

[26] Liedhegner, J. E., Jennings, W., & Wainright, J. (2011). Rapid electrochemical detection of radiolysis products in an aqueous solution exposed to alpha particle beams. *International Journal of Electrochemistry*, 864126 (864129 pp.)-864126 (864129 pp.)864126 (864129 pp.). doi: 10.4061/2011/864126

[27] Lin, C., & Ritter, J. A. (2000). Carbonization and activation of sol-gel derived carbon xerogels. *Carbon, 38*(6), 849-861. doi: 10.1016/s0008-6223(99)00189-x

[28] Liu, W., Li, H., Xu, C., Khatami, Y., & Banerjee, K. (2011). Synthesis of high-quality monolayer and bilayer graphene on copper using chemical vapor deposition. *Carbon, 49*(13), 4122-4130. doi: 10.1016/j.carbon.2011.05.047

[29] Losurdo, M., Giangregorio, M. M., Capezzuto, P., & Bruno, G. (2011). Graphene CVD growth on copper and nickel: role of hydrogen in kinetics and structure. [Article]. *Physical Chemistry Chemical Physics, 13*(46), 20836-20843. doi: 10.1039/c1cp22347j

[30] Musat, R., Moreau, S., Poidevin, F., Mathon, M. H., Pommeret, S., & Renault, J. P. (2010). Radiolysis of water in nanoporous gold. [Article]. *Physical Chemistry Chemical Physics, 12*(39), 12868-12874. doi: 10.1039/c0cp00967a

[31] Pimblott, S. M., LaVerne, J. A., & Mozumder, A. (1996). Monte Carlo simulation of range and energy deposition by electrons in gaseous and liquid water. [Article]. *Journal of Physical Chemistry, 100*(20), 8595-8606. doi: 10.1021/jp9536559

[32] Powell, C. J., & Jablonski, A. (2009). Surface sensitivity of X-ray photoelectron spectroscopy. [Article]. *Nuclear Instruments & Methods in Physics Research Section a-Accelerators Spectrometers Detectors and Associated Equipment, 601*(1-2), 54-65. doi: 10.1016/j.nima.2008.12.103

[33] Pu Sen, W., Wittberg, T. N., & Wolf, J. D. (1988). A characterization of Kapton polyimide by X-ray photoelectron spectroscopy and energy dispersive spectroscopy. *Journal of Materials Science, 23*(11), 3987-39913991.

[34] Royall, C. P., Thiel, B. L., & Donald, A. M. (2001). Radiation damage of water in environmental scanning electron microscopy. *Journal of Microscopy-Oxford, 204*, 185-195. doi: 10.1046/j.1365-2818.2001.00948.x

[35] Scully, S. W. J., Wyer, J. A., Senthil, V., Shah, M. B., & Montenegro, E. C. (2006). Autodissociation of doubly charged water molecules. [Article]. *Physical Review A, 73*(4). doi: 10.1103/PhysRevA.73.040701

[36] Sevik, C., & Bulutay, C. (2007). Theoretical study of the insulating oxides and nitrides: SiO2, GeO2, Al2O3, Si3N4, and Ge3N4. *Journal of Materials Science, 42*(16), 6555-6565. doi: 10.1007/s10853-007-1526-9

[37] Stolyarova, E., Stolyarov, D., Bolotin, K., Ryu, S., Liu, L., Rim, K. T., . . . Flynn, G. (2009). Observation of Graphene Bubbles and Effective Mass Transport under Graphene Films. [Article]. *Nano Letters, 9*(1), 332-337. doi: 10.1021/nl803087x

[38] Swift, J. A., & Brown, A. C. (1970). ENVIRONMENTAL CELL FOR EXAMINATION OF WET BIOLOGICAL SPECIMENS AT ATMOSPHERIC PRESSURE BY TRANSMISSION SCANNING ELECTRON MICROSCOPY. [Note]. *Journal of Physics E-Scientific Instruments, 3*(11), 924-&. doi: 10.1088/0022-3735/3/11/426

[39] Tanuma, S., Powell, C. J., & Penn, D. R. (1991). CALCULATIONS OF ELECTRON INELASTIC MEAN FREE PATHS .2. DATA FOR 27 ELEMENTS OVER THE 50-2000-EV RANGE. *Surface and Interface Analysis, 17*(13), 911-926. doi: 10.1002/sia.740171304

[40] Usami, K., Sakamoto, K., & Ushioda, S. (2001). Influence of molecular structure on anisotropic photoinduced decomposition of polyimide molecules. [Article]. *Journal of Applied Physics, 89*(10), 5339-5342. doi: 10.1063/1.1358323

[41] Vergand, F., Fargues, D., Olivier, D., Bonneviot, L., & Che, M. (1983). ATOMIC-STRUCTURE, SIZE, AND SHAPE OF SMALL NICKEL PARTICLES IN THIN-FILMS. [Article]. *Journal of Physical Chemistry, 87*(13), 2373-2376. doi: 10.1021/j100236a026

[42] Yan, J., Zhao, Z., & Pan, L. (2011). Growth and characterization of graphene by chemical reduction of graphene oxide in solution. *Physica Status Solidi a-Applications and Materials Science, 208*(10), 2335-2338. doi: 10.1002/pssa.201084172

[43] Zakharchenko, K. V., Los, J. H., Katsnelson, M. I., & Fasolino, A. (2010). Atomistic simulations of structural and thermodynamic properties of bilayer graphene. [Article]. *Physical Review B, 81*(23). doi: 10.1103/PhysRevB.81.235439

VITA

Graduate School
Southern Illinois University

Joshua D. Stoll

nu_eden@yahoo.com

Southern Illinois University Carbondale
Bachelor of Science, Physics, December 2009

Thesis Title:

Graphene Membranes as Electron Transparent Windows for Environmental Spectroscopy and Microscopy

Major Professor: Andrei Kolmakov

Publications:

Markevicius, G., Stoll, J. D., Malhotra, V. M., Miller, C. E., & Botha, F. B. (2009). Structural composites from recycled HDPE and calcium sulfite crystallites. *67th Annual Technical Conference of the Society Plastics Engineers 2009*.